

Measuring Object Rotation via Visuo-Tactile Segmentation of Grasping Region

Julio Castaño-Amorós¹ and Pablo Gil²

Abstract—When carrying out robotic manipulation tasks, objects occasionally fall as a result of the rotation caused by slippage. This can be prevented by obtaining tactile information that provides better knowledge on the physical properties of the grasping. In this paper, we estimate the rotation angle of a grasped object when slippage occurs. We implement a system made up of a neural network with which to segment the contact region and an algorithm with which to estimate the rotated angle of that region. This method is applied to DIGIT tactile sensors. Our system has additionally been trained and tested with our publicly available dataset which is, to the best of our knowledge, the first dataset related to tactile segmentation from non-synthetic images to appear in the literature, and with which we have attained results of 95% and 90% as regards Dice and IoU metrics in the worst scenario. Moreover, we have obtained a maximum error of $\approx 3^\circ$ when testing with objects not previously seen by our system in 45 different lifts. This, therefore, proved that our approach is able to detect the slippage movement, thus providing a possible reaction that will prevent the object from falling.

Index Terms—Perception for Grasping and Manipulation, Grasping, Force and Tactile Sensing

I. INTRODUCTION

THE methods employed to carry out robotic manipulation tasks, which are based on 2D/3D vision techniques [1], generally take into account only the geometric properties of objects in the scene. The physical properties of the objects, such as their mass distribution (variable or otherwise), the center of gravity, or friction are not contemplated, signifying that the object could fall if it is not correctly grasped. In contrast, the use of tactile sensors makes it possible to measure and react to these physical properties in order to achieve stable grasping [2].

Several technologies with which to attain a sense of touch and thus find solutions to complex problems such as slip detection have been designed. The most common are electrical-based tactile sensors, such as capacitive, piezoresistive or optical-based tactile sensors [3], on which our work is focused.

Manuscript received: February, 22, 2023; Revised April, 12, 2023; Accepted June, 1, 2023.

This paper was recommended for publication by Editor M. Vincze upon evaluation of the Associate Editor and Reviewers' comments.

This work was supported by the Ministry of Science and Innovation of the Spanish Government through the research project PID2021-122685OB-I00 and by the University of Alicante through the grant UAFPU21-26.

¹Julio Castaño-Amorós is with the AUROVA Lab, Computer Science Research Institute, University of Alicante, Alicante, Spain. julio.ca@ua.es

²Pablo Gil is with the AUROVA Lab, Computer Science Research Institute and with Department of Physics, Systems Engineering, and Signal Theory, University of Alicante, Alicante, Spain. pablo.gil@ua.es

Digital Object Identifier (DOI): see top of this page.

The most typical event to cause an object to fall from human or robotic hands during a manipulation task is probably slippage. In order to achieve a stable grasping while a robotic hand is manipulating an object, it is necessary to obtain and interpret information concerning the contact between the sensor surface and the grasped object. Tactile sensors can, therefore, be used to sense the slippage [4] and the data obtained can then be used to control the movement of the robotic hand. For example, tactile readings have previously been used: to classify the grasping in slip or non-slip states, as shown in [5], to classify the kind of movement (rotation and translation) that takes place when a slippage occurs [6], or to measure displacement by using visual markers on tactile optical sensors [7].

In this paper, we present an algorithm with which to estimate the rotation angle of an object that is being manipulated when slippage occurs. This method is applied to optical DIGIT sensors [8] whose tactile reading is simply an RGB image without visual markers, depth information or force values. Our main contribution is threefold:

- The implementation of a two-stage method based on deep learning and traditional computer vision algorithms in order to segment the contact region and estimate the rotational slippage angle for the task of grasping and lifting an object.
- The generation and public sharing of our tactile segmentation dataset. This is, to the best of our knowledge, the first dataset related to tactile segmentation in literature containing data from real DIGIT sensors, whose objective is to reduce the manual labeling process and encourage the use of learning techniques in order to expand these data to other units of DIGIT sensors.
- Extensive and rigorous experimentation and the comparison of different segmentation neural networks and computer vision algorithms used for the task of tactile segmentation. We also compare our proposal with other state-of-the-art methods for the estimation of the angle of rotational slippage.

This paper is organized as follows: Section II provides a brief introduction to related works regarding contact segmentation and angle estimation for slippage detection, while Section III provides a detailed description of our proposed method and how it differs from the other approaches. Section IV shows two comparisons: one of the different variants of the two stages of our method, and the other of our final proposal and other state-of-the-art methods in literature. Finally, the results obtained are summarized and discussed in Section V, as are the limitations

of this work.

II. RELATED WORK

A. Estimating the Contact Region

Estimating the contact region between the robot’s fingertips and the object being grasped is crucial to the performance of any manipulation task. For example, the objective of the work presented in [9] and [10] was to estimate the contact region by subtracting contact and non-contact tactile images. In [11] and [12], the authors used vision-based tactile sensors with markers to estimate the contact region. In the first case, it was obtained by detecting and grouping the moving markers, while in the second it was estimated through the use of a Gaussian regression model. Other authors, in [13], used synthetic tactile images obtained from simulation to train a Residual NN model of contact recognition for 3D reconstruction of object surfaces. Following a similar line, [14] and [15] solved the contact estimation task for the surface reconstruction between the object and the fingertips implementing photometric algorithms.

Finally, the approach that inspired our work consists of segmenting the contact region with neural networks. In [16], the authors used a vanilla Convolutional Neural Network (CNN) to generate heightmaps from tactile images with the aim of reconstructing the local contact surface. In [17] they used Generative Adversarial Networks (GANs) to segment the region of contact in order to track the contour of the object by applying Reinforcement Learning (RL) techniques.

In contrast, in this work, we use tactile segmentation to calculate the rotation angle of an object when slippage occurs during manipulation tasks. Although our work is inspired by the aforementioned works, the main differences lie in the fact that we use DIGIT sensors without markers [11], [12], which do not produce depth information [14], [15], and state-of-the-art segmentation neural networks, which are more robust than subtracting operations [9], [10] and vanilla CNN [16], and whose training is more stable when compared to the training of GANs [17]. Moreover, in this paper, our methods are trained in order to segment several contact geometries of real household objects, while in [16] the authors trained their CNNs using basic 3D printed geometries, and in [17] they trained an RL agent to follow contours and surfaces by segmenting edges.

B. Slip Detection and Estimation of the Object Rotation

Slippage is a common physical event that occurs during object manipulation, and attempts to solve it have been made for several years. For example, in [18] the authors implemented traditional image preprocessing techniques in order to detect slippage from tactile images. In [19], Long Short-Term Memory (LSTM) neural networks were trained to identify translation, rotation or rolling slip movements from tactile images. In [20], the authors combined CNNs and Recurrent Neural Networks (RNNs) so as to classify slippage in translation, clockwise and counterclockwise rotation from sequential pressure values. A more advanced approach is to quantify the translation or rotation. In this line, [9] used vision-based tactile sensors with markers to calculate the rotation angle from the estimation of the rotation center by employing a least

square algorithm. Another approach consists of exchanging the vision-based sensors for force/torque sensors in order to obtain the rotation angle in a pivoting task as occurs in [21], in which the authors trained RNNs to calculate the pivoting angle from sequential force values.

The work presented in this proposal was inspired by the methods that characterize and quantify the rotational slippage in order to evaluate the performance of different algorithms, which can be combined in the pipeline of our method, for the estimation of the rotation angle from the segmented region of predicted contact. We additionally compare our two-stage method with an end-to-end method for this same task.

III. METHODS

A. Our Method for the Estimation of the Slippage Angle

We propose a two-stage method with which to estimate the angle of rotation caused by slippage during a robotic task concerning the grasping and lifting of an object. Figure 1 shows a scheme that defines the different parts of the two stages of our method. Besides, other algorithms are described to define other approaches to carry out a comparative and ablation study for the validation of our method.

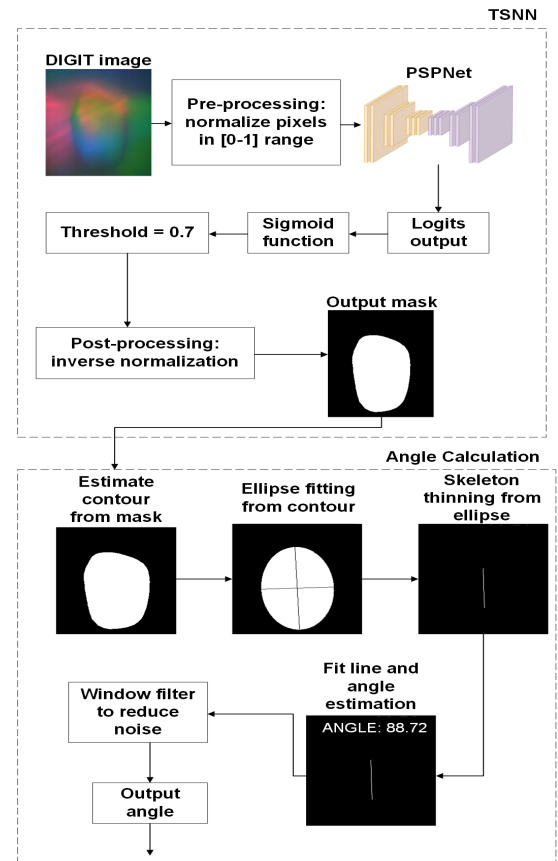


Fig. 1: Scheme of our system combining both stages

The first stage, denominated as Tactile Segmentation Neural Network (TSNN), receives a raw RGB image from a DIGIT sensor as input, which is normalized by scaling the pixel values in a range of between 0 and 1. This normalized image is

sent as input to a PSPNet model [22] that was trained to segment the contact region of the tactile image. A sigmoid activation function is applied so as to transform the output of the PSPNet model, known as logits, into pixel values in a range of [0-1]. Note that this is important in order to later use an empirically obtained restrictive threshold of 0.7 to classify the pixel values from the [0-1] range in two classes: background (0-pixel value) and contact region (1-pixel value). Finally, a post-processing step is carried out, which consists in applying the inverse normalization of the pre-processing step in order to transform the pixel values into a [0-255] range so as to generate the final output mask.

The output mask from the previous stage is used as input in the second stage to obtain the predominant contour present in the image. An ellipse-fitting [23] algorithm is then used to reduce the noise of the segmented output mask, and a Skeleton Thinning [24] algorithm is later applied in order to obtain the main axis of the output mask. This axis can be used to estimate the angle of rotation by fitting a line with a least square process and calculating the arctan function. The angle is processed by a window filter that averages the last n angles in order to produce the mean angle of rotation. This filter helps reduce the noise from the camera's signal, which affects the segmented region by changing its size and shape.

B. Variants of our Method for a Comparative and Ablation Study

As stated previously, our method is made up of two stages: one for the contact region segmentation and another for the estimation of the slippage angle. Our TSNN is based on PSPNet architecture, which extracts a feature map from the last layer of a CNN in order to later process it with a Pyramid Pooling module so as to learn features on different scales, and finally concatenate the original and the processed feature maps in order to generate the output mask. Furthermore, our angle estimation method is based principally on the Skeleton Thinning algorithm, which narrows the contact region into a line by blackening white pixels depending on the neighborhood.

In order to carry out comparative experimentation, two segmentation NNs (DeepLabV3+ [25] and Unet++ [26]) adapted to our task and two angle estimators (Principal Component Analysis (PCA) [27] and Ellipse Fitting [23]) were considered.

On the one hand, DeepLabV3+ and Unet++ architectures differ from the PSPNet architecture since they are based on the encoder-decoder scheme. Moreover, while Unet++ is known for re-designing the skip connections in Unet so as to reduce the semantic gap in order to capture fine-grained details, DeepLabV3+ is characterized by the use of a combination of atrous or dilated convolutions and depthwise separable convolutions, which reduce the computational complexity while maintaining the performance. On the other hand, PCA and Ellipse Fitting differ from Skeleton Thinning since they estimate the angle of slippage by calculating the eigenvalues and eigenvectors. In PCA, the covariance matrix is used to calculate the eigenvalues and eigenvectors in order to identify the principal components of the data. In Ellipse Fitting, the LIN algorithm [23] is applied to estimate the curve that best

fits a set of input points (in our case, the contour points of the segmented region) and its output is the eigenvectors from which the angle is calculated.

The following section, therefore, shows an experimental comparison of our proposal (PSPNet-Skeleton) versus the other eight possible combinations of segmentation (DeepLabV3+, Unet++, our TSNN based on PSPNet) and angle estimators (PCA, Ellipse Fitting, Skeleton Thinning) in the comparative and ablation study.

IV. EXPERIMENTATION AND RESULTS

A. Data Acquisition and Dataset Generation

Although the number of works using visual-based tactile sensors has increased over the last few years, we have been unable to find any dataset related to tactile segmentation containing data from real DIGIT sensors as a basis in our experimentation. We have chosen to work with real instead of synthetic images [13] to avoid losing contact features that can be presented in non-rigid objects and affect the grasping. We have, therefore, generated our own dataset by applying an automatic data recording process with a UR5e robot, a 3F Robotiq gripper, and a visual-based tactile sensor known as DIGIT (see Fig. 2). The recording process consisted of capturing tactile images from the sensors while the robot was grasping an object, each time with a different pose. The grasping force was also varied (range $\approx [0.2-1.8\text{N}]$) depending on the mass, rigidity, type of surface and geometry of the grasping area of the object. Only two fingers were used to grasp the objects in order to test our system in extremely unstable conditions.

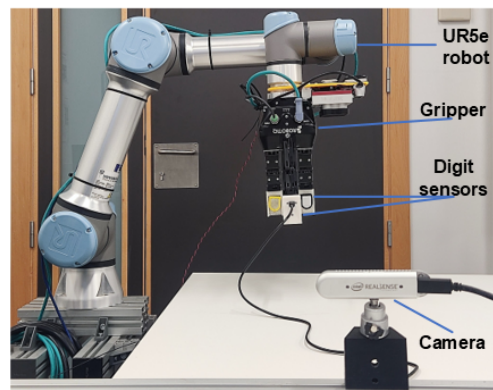


Fig. 2: Setup made up of an external camera, a UR5e robot arm with a 3F Robotiq gripper and DIGIT sensors mounted on the fingertips

Our tactile segmentation dataset was created by using 16 objects (see Fig. 3), and between 200 and 250 tactile images were then captured per object. The objects belong to the YCB dataset [28] and contain different features related to touch sensing, such as texture, rigidity, size, mass, friction, or shape, thus, allowing us to contribute to the repeatability of the experimentation and the benchmarking of tactile manipulation.

We manually defined 15 poses (a combination of 3 positions and 5 orientations) per object, and ensure that our DIGIT

sensor was capturing different geometries from the local contact with the object. This number of poses per object was, therefore, sufficient to form our dataset owing to the uniformity and symmetry of the surfaces of the objects. The variability of objects and poses thus enabled the neural networks trained with our dataset to achieve high generalization capabilities. The black rectangles in Fig. 3 represent the grasping areas established in order to record our dataset so as to capture a large variety of tactile images with different contact geometries. The bigger boxes represent a higher percentage of grasping actions in this area.

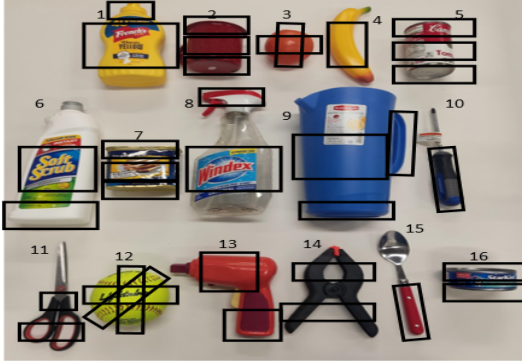


Fig. 3: Objects from YCB dataset used to generate our tactile segmentation dataset. [Link to download dataset](#)

In this work, we have formulated the tactile segmentation task as a supervised learning problem, signifying that it was necessary to label our data. This was done by using the LabelMe tool [29] to label the contact regions on the tactile samples. The labeling process was carried out manually by observing the contact images with respect to a non-contact image reference.

The initial tactile segmentation dataset, which contains a total of 3675 images, was then used to generate three sets (D_{s1} , D_{s2} , and D_{s3}) by applying the 3-fold cross-validation technique. This was done in order to carry out an optimal evaluation of our models. We randomly split each set by following a distribution of 70% of the objects (11 objects) for training, 20% (3) for validation, and 10% (2) for testing. Table I shows the corresponding identifiers of the objects shown in Fig. 3 for each set.

TABLE I: 3-fold cross-validation technique and mapping between our tactile segmentation dataset and object’s identifiers

| | D_{s1} | D_{s2} | D_{s3} |
|-----------------------|--------------------------------------|--------------------------------------|-------------------------------------|
| Train set | 1, 2, 4, 5, 6, 8, 10, 12, 13, 14, 15 | 1, 2, 3, 4, 6, 7, 10, 11, 12, 13, 16 | 1, 3, 5, 6, 7, 8, 9, 10, 11, 13, 14 |
| Validation set | 7, 9, 11 | 5, 9, 14 | 4, 15, 16 |
| Test set | 3, 16 | 8, 15 | 2, 12 |

B. Performance Evaluation of our Proposal vs. other Approaches

The performance of the trained models was evaluated using the *Dice* and *IoU* scores, which are described in Eqs. 1 and 2, respectively.

$$Dice = \frac{2 * pred * y}{pred + y} \quad (1)$$

$$IoU = \frac{pred * y}{pred + y - pred * y} \quad (2)$$

where *pred* are the images containing the predicted contact regions and *y* are the images with the labeled contact regions. The *Dice* score is a metric that is similar to the average performance, while the *IoU* score is more like the worst-case scenario.

The training phase was carried out employing an NVIDIA A100 Tensor Core GPU with 40 GB of RAM, along with the following optimal hyperparameters obtained from a process of searching and tuning: a batch size of 32, a learning rate of $1e-4$, the Adam optimizer, the Focal loss, 30 training epochs and a ResNet18 backbone. We also trained with the EfficientNet-B3 backbone, but as ResNet18 achieved higher metric values in all of the training sessions, we have not included the experimental results in our work. ResNet architecture is well-known for the residual blocks that help reduce the vanishing gradient problem in deep neural networks. The testing phase was carried out using an NVIDIA GeForce GTX 1650 Ti with 4GB of RAM to perform the comparison regarding real-time capabilities.

Table II shows the results of the testing phase in terms of the *Dice*, *IoU* and time values when our TSNN was compared to the other approaches adapted to the task using each set (D_{s1} , D_{s2} , and D_{s3}) of our dataset.

TABLE II: Segmentation results for the sets D_{s1} , D_{s2} , and D_{s3} comparing our TSNN with Unet++ and DeepLabV3+, using the ResNet18 backbone

| Unet++ | | | |
|----------------------------|-------------------------------------|-------------------------------------|-------------------------------------|
| | Dice | IoU | Time(s) |
| D_{s1} | 0.950 ± 0.018 | 0.906 ± 0.033 | 0.008 ± 0.001 |
| D_{s2} | 0.955 ± 0.008 | 0.915 ± 0.015 | 0.009 ± 0.002 |
| D_{s3} | 0.969 ± 0.006 | 0.940 ± 0.011 | 0.009 ± 0.001 |
| Avg | 0.958 ± 0.011 | 0.920 ± 0.020 | 0.009 ± 0.001 |
| DeepLabV3+ | | | |
| | Dice | IoU | Time(s) |
| D_{s1} | 0.947 ± 0.020 | 0.899 ± 0.036 | 0.007 ± 0.002 |
| D_{s2} | 0.951 ± 0.012 | 0.906 ± 0.021 | 0.006 ± 0.002 |
| D_{s3} | 0.969 ± 0.007 | 0.937 ± 0.013 | 0.006 ± 0.002 |
| Avg | 0.956 ± 0.013 | 0.914 ± 0.023 | 0.006 ± 0.002 |
| TSNN | | | |
| | Dice | IoU | Time(s) |
| D_{s1} | 0.937 ± 0.026 | 0.883 ± 0.045 | 0.007 ± 0.003 |
| D_{s2} | 0.953 ± 0.009 | 0.910 ± 0.017 | 0.006 ± 0.003 |
| D_{s3} | 0.963 ± 0.008 | 0.929 ± 0.014 | 0.006 ± 0.001 |
| Avg | 0.951 ± 0.014 | 0.907 ± 0.025 | 0.006 ± 0.002 |

It will be first noted that the *Dice* scores are higher than the *IoU* scores in every case. It will be also noted that the difference in the average offline inference time is not significant, signifying that the three neural architectures can make predictions in real time. Finally, note that all the approaches, including our TSNN, achieve higher metric values with the D_{s3} set. This may be for several reasons, such as

the fact that the objects in the D_{s3} test set are easier to segment than are those in the other test sets. However, there are no significant differences in the difficulty of segmenting the objects from each set. We consequently believe that the D_{s3} set contains a better distribution of contact surfaces that yield higher metric values. We therefore decided that the weights obtained from the training with the D_{s3} set would be used for the study and comparison of our TSNN versus the remaining segmentation approaches. Figure 4 shows examples of our tactile segmentation with different samples from the test sets.

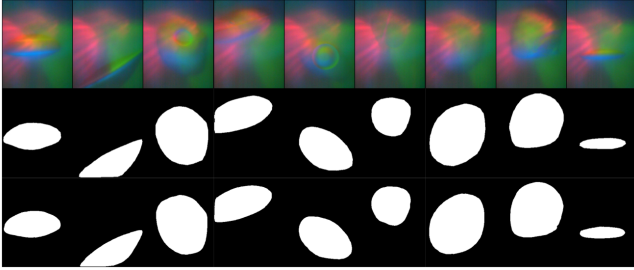


Fig. 4: Examples of tactile segmentation made by our TSNN. The first row corresponds to the raw tactile images, the second row is the ground truth segmented images and the third row corresponds to the predicted contact region

The performance was evaluated by implementing the task of grasping and lifting an object while our system carried out the tactile segmentation and angle calculation of the segmented contact region. As shown in Fig. 5, this task is divided into three parts: the first when the robot grasps the object, the second when the robot lifts it, and the last when the robot holds it on one side. In this work, we focus solely on the second part (part B in Fig. 5) because this is where the slippage movement may occur.

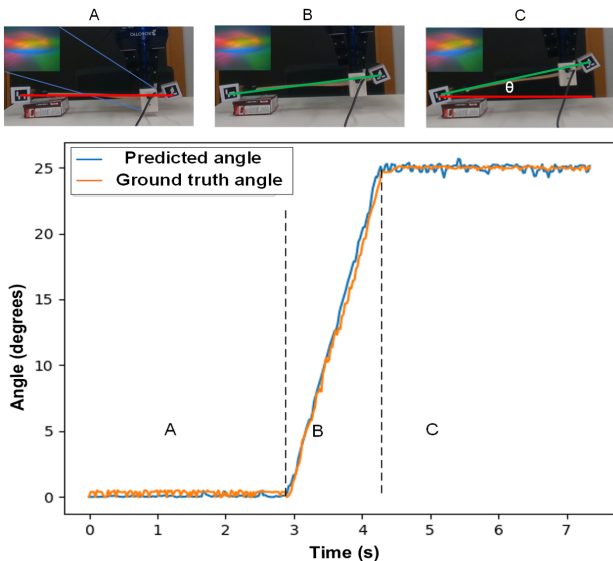


Fig. 5: Description of rotation angle calculation during the manipulation task with object 2 from our set of experimentation

Figure 5 shows the predicted angle in blue and the ground truth angle in orange. The predicted angle is calculated as

being the difference between the current and the initial angle obtained from the methods described in Section III. The ground truth angle θ is obtained with the formula described in Eq. 3, where \vec{p} is the current vector (green line) and \vec{q} is the initial vector (red line) that links the two ArUco markers.

$$\theta = \text{acos}\left(\frac{\vec{p} \cdot \vec{q}}{|\vec{p}| \cdot |\vec{q}|}\right) \quad (3)$$

The noise from the camera's signal affects the segmented region, thus making the angle calculation noisier. We therefore applied a filtering window that consisted of calculating the mean of n consecutive angles (predicted angle).

We validated our system by randomly selecting two objects from our dataset, concretely, objects 1 and 7 from Fig. 3, and testing it with seven unseen objects (1 to 7 in Fig. 6). These nine objects form the dataset (D_a) for the slip angle experimentation, which differs from the dataset shown in Fig. 3 because the objective was to test our proposal with new objects and grasping surfaces.

The experimentation consisted of making five lifts per object (45 in total) while calculating the **Rotational Error (RE)** as the absolute difference in degrees between the predicted and ground truth angles. The results have been divided into two parts.

First, a comparative and ablation study was carried out with the proposed method and the other eight possible approaches from Section III-B. In this study, the **Mean Absolute Rotational Error (MARE)** was calculated for each of the 9 methods, varying the size of the window filter from 2 to 10 with a step of 2, as can be seen in Table III. In order to compute the MARE, we calculated the mean RE and standard deviation for each of the 45 lifts with each method and window size n . We then computed the average of these 45 mean REs and standard deviations in order to obtain the MARE. Note that a 2-size window filter yields the lowest MARE for every method. Increasing the window size does not improve the results because when we increase the window size, the noise is filtered, but the angle magnitude is reduced, thus increasing the error between the predicted and ground truth angle. The Skeleton algorithm obtained the lowest MARE with all segmentation methods, no matter which window size, obtaining almost half the error of the other angle approaches. This is because the Skeleton algorithm simplifies the segmented contact region to a single line and does not, therefore, calculate the angle directly from the segmented mask as the PCA and Ellipse approaches do. Small changes in size or translations of the segmented contact region consequently affect the angle calculation to a lesser extent. In summary, the MAREs obtained are similar, although the results obtained with our proposal when combining a TSNN based on PSPNet and Skeleton Thinning are slightly better.

Having proved which method and window size is optimal, we now show the RE for the 5 lifts of each object in the boxplot graphic in Fig. 6.

Note that the horizontal yellow lines represent the median RE, the box represents the interquartile range and the vertical lines represent the minimum and maximum REs. Overall, our proposal achieves a MARE of $1.85^\circ \pm 0.96^\circ$ (see Table III),

TABLE III: Comparison of our proposal, TSNN based on PSPNet and Skeleton Thinning, versus the rest of the approaches

| Method | Window Size | | | | |
|--------------------------------|---|---|---|---|---|
| | 2 | 4 | 6 | 8 | 10 |
| DeepLabV3+ and PCA | $3.52^{\circ} \pm 1.71^{\circ}$ | $3.81^{\circ} \pm 1.66^{\circ}$ | $4.13^{\circ} \pm 1.61^{\circ}$ | $4.42^{\circ} \pm 1.55^{\circ}$ | $4.76^{\circ} \pm 1.52^{\circ}$ |
| DeepLabV3+ and Ellipse | $2.82^{\circ} \pm 1.40^{\circ}$ | $3.06^{\circ} \pm 1.37^{\circ}$ | $3.36^{\circ} \pm 1.36^{\circ}$ | $3.65^{\circ} \pm 1.32^{\circ}$ | $3.97^{\circ} \pm 1.32^{\circ}$ |
| DeepLabV3+ and Skeleton | $1.85^{\circ} \pm 0.99^{\circ}$ | $2.02^{\circ} \pm 0.96^{\circ}$ | $2.18^{\circ} \pm 0.97^{\circ}$ | $2.37^{\circ} \pm 1.01^{\circ}$ | $2.62^{\circ} \pm 1.04^{\circ}$ |
| UNET++ and PCA | $3.48^{\circ} \pm 1.62^{\circ}$ | $3.78^{\circ} \pm 1.59^{\circ}$ | $4.05^{\circ} \pm 1.56^{\circ}$ | $4.33^{\circ} \pm 1.50^{\circ}$ | $4.66^{\circ} \pm 1.47^{\circ}$ |
| UNET++ and Ellipse | $2.93^{\circ} \pm 1.40^{\circ}$ | $3.17^{\circ} \pm 1.39^{\circ}$ | $3.43^{\circ} \pm 1.39^{\circ}$ | $3.72^{\circ} \pm 1.36^{\circ}$ | $4.03^{\circ} \pm 1.36^{\circ}$ |
| UNET++ and Skeleton | $1.90^{\circ} \pm 0.90^{\circ}$ | $2.01^{\circ} \pm 0.93^{\circ}$ | $2.20^{\circ} \pm 0.95^{\circ}$ | $2.44^{\circ} \pm 0.99^{\circ}$ | $2.67^{\circ} \pm 1.06^{\circ}$ |
| PSPNet and PCA | $3.56^{\circ} \pm 1.71^{\circ}$ | $3.86^{\circ} \pm 1.67^{\circ}$ | $4.18^{\circ} \pm 1.63^{\circ}$ | $4.50^{\circ} \pm 1.57^{\circ}$ | $4.81^{\circ} \pm 1.54^{\circ}$ |
| PSPNet and Ellipse | $2.90^{\circ} \pm 1.39^{\circ}$ | $3.14^{\circ} \pm 1.37^{\circ}$ | $3.42^{\circ} \pm 1.37^{\circ}$ | $3.72^{\circ} \pm 1.35^{\circ}$ | $4.02^{\circ} \pm 1.37^{\circ}$ |
| Proposed method | $1.85^{\circ} \pm 0.96^{\circ}$ | $2.02^{\circ} \pm 0.94^{\circ}$ | $2.19^{\circ} \pm 0.97^{\circ}$ | $2.41^{\circ} \pm 1.03^{\circ}$ | $2.63^{\circ} \pm 1.09^{\circ}$ |

signifying that our approach estimates the angle of rotational slippage with a maximum MARE of 2.81° in the worst case. Note that the maximum REs are obtained when testing with the objects 5 and 7. This is owing to the geometry of the grasping surface and the segmented region of contact. However, these maximum REs are isolated cases of one of the 5 lifts.

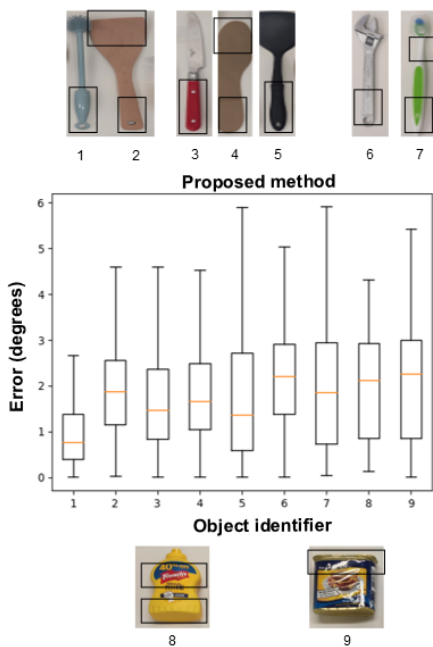


Fig. 6: REs for each object using the proposed method (PSPNet and Skeleton Thinning) with a window size of 2

Following the same guidelines described above, the black rectangles in Fig. 6 represent the different areas of the objects used as the grasping contact origin for the different trials. Note that we set up the contact origins in an attempt to reproduce the way in which a human operator would do so by, for example, avoiding dangerous areas of the objects such as the sharp part of the knife.

Figures 5 and 7 show some examples of RE calculation using our two-stage method with different objects. Note that the slippage angle varies in a range between of 0° and 30° for all the lifts because we have limited the angle measurement

considering that a robot should react before the slippage angle becomes this value in order to prevent the object from falling.

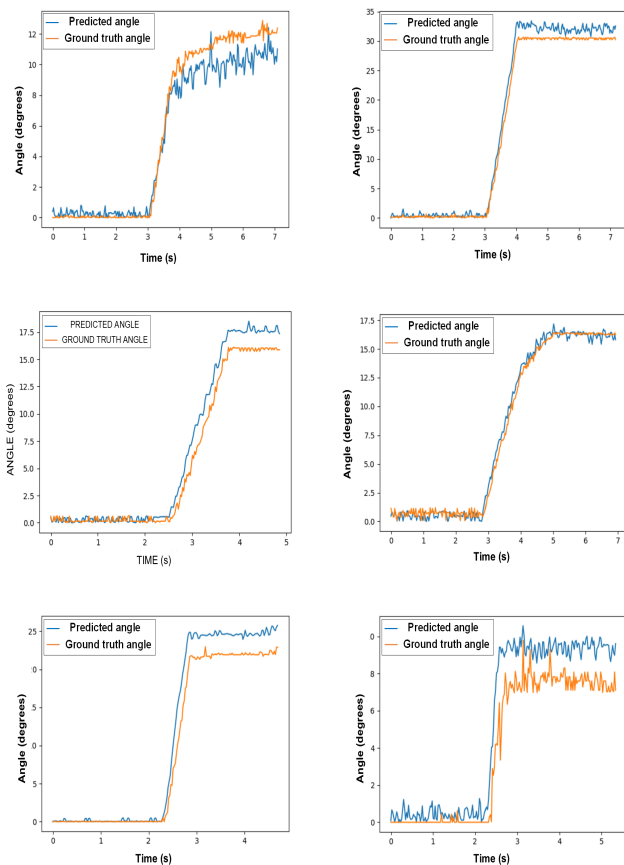


Fig. 7: Examples of REs calculation for slipping during lift task with different objects from Fig. 6. First row: objects 1, 3. Second row: 4, 5. Third row: objects 6, and 7

The error of the measurement depends on many factors, such as the contact shape, the mass and geometry of the object, etc. The error obviously also depends on the magnitude of the slippage, which is usually higher when the slippage magnitude is higher, but it is not directly related, as can be observed in the case of the objects 5 and 7 in Fig. 7. In this case, object 7 gets

a higher error due to a small distance between the grasping pose and the center of mass of the object.

C. Objective and Subjective Comparison of our proposal vs State-of-the-Art Methods

As it is complex to find benchmarks for the proposed task because of the variability of data and sensors, we carried out two comparisons. First, a subjective comparison between the proposed method and two other works [9], [21] was performed. This comparison was subjective owing to the fact that we were unable to reproduce the results obtained in the aforementioned studies because the sensors employed were not available, although the test was carried out with the same or similar objects. Second, we show the results of an objective comparison of our work with another [30]. Here, objective signifies that we implemented our own version of the other authors' work in order to reproduce their results and compare them with ours using the exact same objects and data, as their code was not available.

On the one hand, [9] approached the task of slip detection using vision-based tactile sensors containing visual markers and a least-square algorithm, while [21] employed force tactile sensors and RNNs to predict the pivoting angle during slippage. Although we did not carry out the test with the exact set of objects, it was possible to make a subjective comparison in order to prove that competitive results could be attained for this task while using poorer tactile readings, such as only an RGB image. The comparison is shown in the right-hand column of Table IV.

On the other hand, [30] presented an NN denominated AngleNet, based on the ConvNext neural architecture, that was used to predict the rotation angle, from DIGIT images, with respect to the vertical axis of tubular objects in Sim-to-Real tasks. In order to compare AngleNet with our work in the most competitive scenario, we trained it with the 45 lifts from our previous experimentation, and we also tested it with the training data so as to obtain the results in the best possible case. The results obtained are shown in the left-hand column of Table IV. The higher error of AngleNet may be owing to the fact that in an end-to-end approach it is harder to estimate the angle from the tactile reading without knowing where the contact shape is and what it is like.

TABLE IV: Objective and subjective comparison of the proposed method and other state-of-the-art approaches regarding MARE error and standard deviation

| | Objective | Subjective |
|-------------|---|---|
| [9] | - | $4.39^\circ \pm 0.18^\circ$ |
| [21] | - | $3.96^\circ \pm \text{UNK}$ |
| [30] | $3.23^\circ \pm 1.69^\circ$ | - |
| Ours | $1.85^\circ \pm 0.96^\circ$ | $1.85^\circ \pm 0.96^\circ$ |

D. Discussion and Limitations of our Method

Although this work proves that our approach achieves promising results, our system also has limitations. For example, when the segmented contact region is like a circle. In

this case, our proposed method converts a circular mask into a single point rather than a line after applying the Skeleton transformation, as described in Fig. 8, and the predicted angle is not, therefore, reliable. This limitation could be solved by using a vision system that calculates the grasping points on a surface with a low curvature or edge. In Fig. 9, we show how the angle calculation varies depending on the grasping surface by using two different objects from Fig. 8. If the surface is like an edge, the results are promising, but the calculation of the angle is less reliable with surfaces with large curvature. Non-homogeneous objects which generate non-continuous contact shapes are also a limitation, although only closed contact shapes are considered in this work.

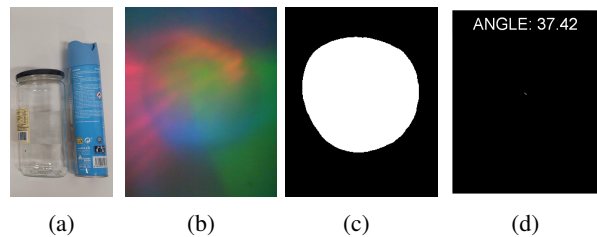


Fig. 8: Example of angle calculation when the segmented contact region is almost circular

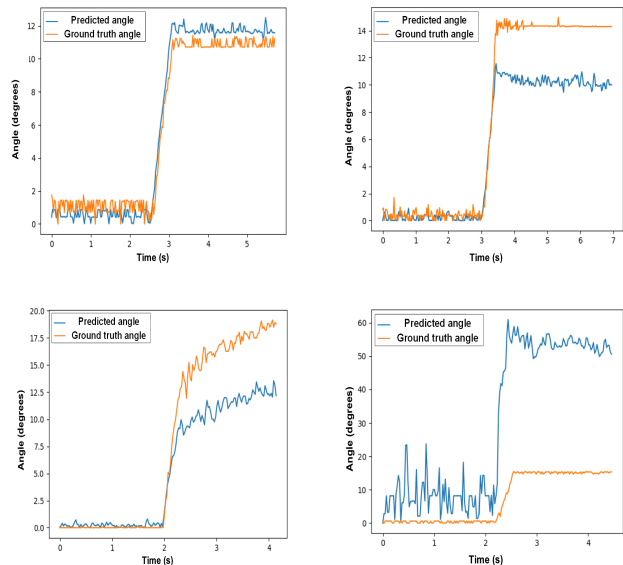


Fig. 9: Angle calculation with different grasping surfaces. First row: edge surface, second row: cylindrical surface

V. CONCLUSIONS

In this proposal, we propose a two-stage system with which to measure the rotation angle caused by slippage events when we work with DIGIT tactile sensors whose tactile reading is an RGB image. Our proposal uses TSNN based on PSPNet to obtain the local contact region between the robot's fingertips and the manipulated object, after which the Skeleton Thinning algorithm estimates the rotation angle. Our method achieves a

MARE of $1.85^\circ \pm 0.96^\circ$ when subjectively compared with the error of $3.96^\circ \pm \text{UNK}$ in [9] and the error of $4.39^\circ \pm 0.18^\circ$ in [21], and objectively compared with the error of $3.23^\circ \pm 1.69^\circ$ in [30]. Moreover, the code is available at [github link](#) and a demo is shown in the following [video link](#). Our system also has some limitations regarding the shape of the contact region. When this shape is nearly a circle, it is impossible to estimate its rotation movement. In this case, we propose to grasp the object by surfaces with a small curvature and show how this improves the results in comparison with large curvature surfaces. On the other hand, objects such as a spiked ball, which generate more than one contact shape, would make the estimated angle less reliable. In addition, as future work, we are working on solving these two limitations to expand our method to detect slippage when grasping more complex objects.

REFERENCES

- [1] G. Du, K. Wang, S. Lian, and K. Zhao, "Vision-based robotic grasping from object localization, object pose estimation to grasp estimation for parallel grippers: a review". *Artificial Intelligence Review*, vol. 54, pp. 1677–1734, 2021, doi: 10.1007/s10462-020-09888-5
- [2] S. Luo, J. Binbo, R. Dahiya and H. Liu, "Robotic tactile perception of object properties: A review". *Mechatronics*, vol. 48, pp. 54-67, 2017, doi: 10.1016/j.mechatronics.2017.11.002
- [3] S. Zhang et al., "Hardware Technology of Vision-Based Tactile Sensor: A Review," *IEEE Sensors Journal*, vol. 22, no. 22, pp. 21410-21427, 2022, doi: 10.1109/JSEN.2022.3210210
- [4] W. Chen, H. Khamis, I. Birznieks, N. F. Lepora and S. J. Redmond, "Tactile Sensors for Friction Estimation and Incipient Slip Detection—Toward Dexterous Robotic Manipulation: A Review," *IEEE Sensors Journal*, vol. 18, no. 22, pp. 9049-9064, 2018, doi: 10.1109/JSEN.2018.2868340.
- [5] R. A. Romeo, C. Lauretti, C. Gentile, E. Guglielmelli and L. Zollo, "Method for Automatic Slippage Detection With Tactile Sensors Embedded in Prosthetic Hands," *IEEE Transactions on Medical Robotics and Bionics*, vol. 3, no. 2, pp. 485-497, 2021, doi: 10.1109/TMRB.2021.3060032.
- [6] A. Grover, P. Nadeau, C. Grebe and J. Kelly, "Learning to Detect Slip with Barometric Tactile Sensors and a Temporal Convolutional Neural Network," in *IEEE Int. Conf. on Robotics and Automation (ICRA)*, Philadelphia, USA, 2022, pp. 570-576, doi: 10.1109/ICRA46639.2022.9811592.
- [7] W. Yuan, R. Li, M. A. Srinivasan and E. H. Adelson, "Measurement of shear and slip with a GelSight tactile sensor," in *IEEE Int. Conf. on Robotics and Automation (ICRA)*, Seattle, USA, 2015, pp. 304-311, doi: 10.1109/ICRA.2015.7139016.
- [8] M. Lambeta, P-W. Chou, S. Tian, B. Yang, B. Maloon, V. R. Most, D. Stroud, R. Santos, A. Byagowi, G. Kammerer, D. Jayaraman and R. Calandra, "DIGIT: A Novel Design for a Low-Cost Compact High-Resolution Tactile Sensor With Application to In-Hand Manipulation," *IEEE Robotics and Automation Letters*, vol. 5, no. 3, pp. 3838-3845, 2020, doi: 10.1109/LRA.2020.2977257
- [9] R. Kolamuri, Z. Si, Y. Zhang, A. Agarwal, and W. Yuan, "Improving Grasp Stability with Rotation Measurement from Tactile Sensing," in *IEEE/RSJ Int. Conf. on Intelligent Robots and Systems (IROS)*, Prague, Czech Republic, 2021, pp. 6809-6816, doi: 10.1109/IROS51168.2021.9636488
- [10] M. Lambeta, H. Xu, J. Xu, P. W. Chou, S. Wang, T. Darrell, and R. Calandra, "PyTouch: A Machine Learning Library for Touch Processing," in *IEEE Int. Conf. on Robotics and Automation (ICRA)*, Xi'an, China, 2021, pp. 13208-13214, doi: 10.1109/ICRA48506.2021.9561084
- [11] Y. Ito, Y. Kim, G. Obinata, "Contact Region Estimation Based on a Vision-Based Tactile Sensor Using a Deformable Touchpad," *Sensors*, vol.14, no. 4, pp. 5805-5822, 2014, doi: 10.3390/s140405805
- [12] V. Kakani, X. Cui, M. Ma, H. Kim, "Vision-Based Tactile Sensor Mechanism for the Estimation of Contact Position and Force Distribution Using Deep Learning". *Sensors*, vol. 21, no. 5, pp. 1920, 2021, doi: 10.3390/s21051920
- [13] S. Sudharshan, S. Zilin, S. Anderson, M. Kaess, and M. Mustafa, "Monte-Carlo inference over distributions across sliding touch," in *Conf. on Robot Learning (CoRL)*, Auckland, New Zealand, 2023, pp. 319–331
- [14] I. H. Taylor, S. Dong and A. Rodriguez, "GelSlim 3.0: High-Resolution Measurement of Shape, Force and Slip in a Compact Tactile-Sensing Finger," in *Int. Conf. on Robotics and Automation (ICRA)*, Philadelphia, USA, 2022, pp. 10781-10787, doi: 10.1109/ICRA46639.2022.9811832
- [15] S. Wang, Y. She, B. Romero and E. Adelson, "GelSight Wedge: Measuring High-Resolution 3D Contact Geometry with a Compact Robot Finger," in *IEEE Int. Conf. on Robotics and Automation (ICRA)*, Xi'an, China, 2021, pp. 6468-6475, doi: 10.1109/ICRA48506.2021.9560783
- [16] M. Bauza, O. Canal and A. Rodriguez, "Tactile Mapping and Localization from High-Resolution Tactile Imprints," in *Int. Conf. on Robotics and Automation (ICRA)*, Montreal, Canada, 2019, pp. 3811-3817, doi: 10.1109/ICRA.2019.8794298
- [17] Y. Lin, J. Lloyd, A. Church and N. F. Lepora, "Tactile Gym 2.0: Sim-to-Real Deep Reinforcement Learning for Comparing Low-Cost High-Resolution Robot Touch," *IEEE Robotics and Automation Letters*, vol. 7, no. 4, pp. 10754-10761, 2022, doi: 10.1109/LRA.2022.3195195
- [18] J. Castaño-Amorós, I. de L. Páez-Ubieta, P. Gil, S. Puente, "Visual-tactile manipulation to collect household waste in outdoor". *Revista Iberoamericana de Automática e Informática Industrial*, pp. 1-12, 2022, doi: 10.4995/riai.2022.18534
- [19] Y. Zhang, W. Yuan, Z. Kan, and M.Y. Wang, "Towards Learning to Detect and Predict Contact Events on Vision-based Tactile Sensors," in *Conf. on Robot Learning (CoRL)*, Virtual Conference, 2020, pp. 1395-1404
- [20] B.S. Zapata-Impata, P. Gil and F. Torres, "Learning Spatio Temporal Tactile Features with a ConvLSTM for the Direction Of Slip Detection" *Sensors*, vol. 19, no. 523, 2019, doi: 10.3390/s19030523
- [21] J. Toskov, R. Newbury, M. Mukadam, D. Kulić, and A. Cosgun, "In-Hand Gravitational Pivoting Using Tactile Sensing", arXiv preprint arXiv:2210.05068, 2002
- [22] H. Zhao, J. Shi, X. Qi, X. Wang, and J. Jia, "Pyramid Scene Parsing Network," in *IEEE Conf. on Computer Vision and Pattern Recognition (CVPR)*, Honolulu, USA, 2017, pp. 6230-6239, doi: 10.1109/CVPR.2017.660
- [23] A. W. Fitzgibbon, and R. B. Fisher, "A buyer's guide to conic fitting," Edinburgh, UK: University of Edinburgh, Department of Artificial Intelligence, 1996, pp. 513-522
- [24] Z., GUO and R. W., HALL, "Parallel thinning with two-subiteration algorithms," *Communications of the ACM*, 1989, vol. 32, no. 3, pp. 359-373, doi: 10.1145/62065.62074
- [25] L. C. Chen, Y. Zhu, G. Papandreou, F. Schroff, and H. Adam, "Encoder-decoder with atrous separable convolution for semantic image segmentation," in *European Conf. on Computer Vision (ECCV)*, Munich, Germany, 2018, pp. 801-818, doi: 10.1007/978-3-030-01234-2_49
- [26] Z. Zhou, M.M. Rahman Siddiquee, N. Tajbakhsh, J. Liang. "UNet++: A Nested U-Net Architecture for Medical Image Segmentation," *Lecture Notes in Computer Science*, vol 11045. Springer, Cham, 2018, doi: 10.1007/978-3-030-00889-5_1
- [27] F.R.S. Karl Pearson, "LIII. On lines and planes of closest fit to systems of points in space". *The London, Edinburgh, and Dublin Philosophical Magazine and Journal of Science*, 1901, vol. 2, no. 11, pp. 559–572, doi: 10.1080/14786440109462720
- [28] B. Calli, A. Singh, A. Walsman, P Srinivasa S. and, Abbeel, and A. M. Dollar. "The ycb object and model set: Towards common benchmarks for manipulation research," in *Int. Conf. on Advanced Robotics (ICAR)*, Istanbul, Turkey, 2015, pp. 510–517, doi: 10.1109/ICAR.2015.7251504
- [29] K. Wada, "Labelme: Image Polygonal Annotation with Python". Retrieved November 7, 2018, from <https://github.com/wkentaro/labelme>
- [30] Y. Zhao, X. Jing, K. Qian, D. F. Gomes, and S. Luo. "Skill generalization of tubular object manipulation with tactile sensing and Sim2Real learning," *Robotics and Autonomous Systems*, vol. 160, pp. 104321, 2023, doi: 10.1016/j.robot.2022.104321